Large Eddy Simulation of the Wakes of Three Urban Air Mobility Vehicles

Denis-Gabriel Caprace
Postdoctoral Fellow

Andrew Ning
Associate Professor

Brigham Young University
Provo, UT, USA

ABSTRACT

Recent advances in urban air mobility have driven the development of many new VTOL concepts. These vehicles often feature original designs and futuristic shapes. Due to their novelty, the wake characteristics of such aircraft are unknown. However, large wake-induced velocities, should they exist, may be dangerous for any other vehicle evolving in their close proximity. Therefore, improved knowledge about the wakes of VTOL vehicles is needed to guarantee the safety of urban air mobility operations. In this work, we study the wake of three VTOL aircraft in cruise by means of large eddy simulation. We present a two-stage numerical procedure that enables the simulation of long wake ages at a limited computational cost. The analysis of our simulation results reveals that the wakes of rotary vehicles feature larger wake vortex cores than a typical airplane wing. The vortex circulation decay is also faster due to the self-induced turbulence generated during the wake roll-up. Finally, we introduce a model of the vortex circulation distribution that fits the numerical measurements with satisfactory agreement across space and time, and can be used to evaluate induced velocities.

NOTATION

b	$[m]$	:	vehicle span
b_0	$[m]$	:	reference vortex spacing
b_w	$[m]$	:	measured vortex spacing
c_z	$[-]$	:	local sectional force coefficient (vertical)
D	$[m]$	:	rotor diameter
h	$[m]$	:	grid spacing
I_0	$[m^3\,s^{-1}]$	:	reference wake impulse
I_w	$[m^3\,s^{-1}]$	:	measured wake impulse
R	$[m]$	:	rotor radius
R^*	$[m]$	:	wake vortex outer radius
r_c	$[m]$	:	wake vortex core radius
T_0	$[s]$	:	reference vortex descent time
U_∞	$[m/s]$	:	free stream velocity
x_s	$[m]$	:	location of the slice connecting the S-D to the T-D simulation
Γ	$[m^2\,s^{-1}]$	:	wake vortex circulation distribution
Γ^*	$[m^2\,s^{-1}]$	:	wake vortex total circulation
Γ_0	$[m^2\,s^{-1}]$	:	wake reference circulation
Γ_w	$[m^2\,s^{-1}]$	:	wake measured circulation
ρ	$[kg\,m^{-3}]$	:	air density
ψ	$[-]$	:	blade azimuth angle
$\bar{\omega}_x$	$[s^{-1}]$	:	average streamwise vorticity

INTRODUCTION

With the development of Urban Air Mobility (UAM), one foresees that a large number of Unmanned Aircraft System (UAS) will operate in close proximity over densely populated areas in the near future. The safety of both riders and inhabitants will depend upon dedicated traffic management that should ensure the proper separation between all potentially autonomous vehicles, as underlined by Bharadwaj et al. (Ref. 1). To date, one of the uncertainties in the establishment of a reliable UAS Traffic Management (UTM) lies in the determination of safe separation distances discussed in Refs. 2, 3. Similarly to air traffic, these distances must account for the aerodynamic wakes produced by the UAS and their dissipation over time to avoid wake vortex encounters.

However, because of their innovative multi-rotor (e)VTOL designs, the wake generation processes of UAS are not well known. Examples of such vehicles are the NASA UAM vehicle concepts (Fig. 1) presented by Silva et al. (Ref. 4) and Johnson et al. (Ref. 5). In particular, the far wake properties of these vehicles might substantially differ from conventional aircraft since they feature varied arrangements of wings and rotors. It is therefore necessary to collect data on the wakes of such multi-rotor (e)VTOL vehicles to better understand the effect of the vehicle design on the wake. The purpose of this paper is to provide simulation data on UAS wakes to further advance our understanding of the related wake-generation mechanisms and to inform the development of adapted wake models.

Indeed, traffic management would benefit from simplified models of the aerodynamic interaction between UAS, as discussed by Nguyen (Ref. 7). The underlying motivation is the necessity for quick evaluation of wake-induced velocities, as they should be accounted for in the determination of safe trajectories. This, in turn, calls for simplified models of the wake of UAS parametrized by the vehicle design characteris-

Presented at the Vertical Flight Society's 78th Annual Forum & Technology Display, Ft. Worth, Texas, USA, May 10–12, 2022.

Figure 1: Three UAM vehicle concepts proposed by NASA: quadcopter (left), lift plus cruise (center) and side-by-side (right) configurations. The lift plus cruise vehicle is shown in hover mode. In cruise, the wing and rotors ensemble is tilted down and resemble a conventional airplane. The other configurations operate in cruise as shown. Figure reproduced from Ref. 6.

tics and operating conditions, and predicting a realistic wake decay. Currently though, due to the lack of knowledge about UAS wakes, wake models can only be extrapolated from other types of designs (i.e., conventional airplanes or helicopters, as in Ref. 8), causing a risk of inaccurate predictions.

Even though the aerodynamics of compound helicopters (in some ways similar to UAS) have been extensively studied in the past, the focus has rarely been on their far wakes. Previous studies have identified the crucial roles of near-wake rotor-rotor and rotor-airframe interactions in the aircraft aeromechanics (see e.g Ref. 9, and more recently, Ref. 10). Rotors in tandem have been studied separately, for example in the recent work by Pinti et al. (Ref. 11), as it pertains to many drone and UAS configurations. Recently, high resolution CFD by Ventura Diaz et al. and Ventura Diaz and Yoon has brought new insights into the aerodynamics of UAM vehicle concepts (Refs. 12, 13). Specially focused on forward flight —the condition that the present study is concerned with— these studies further emphasized the influence of the fine vortical structures generated by the rotors on the rest of the vehicle aerodynamics. They also revealed details on the topology of the near wake.

Remarkably, the far wake of full-scale helicopters has been studied experimentally by Teager et al. (Ref. 14) who measured wake-induced velocities. More recently, Caprace et al. (Ref. 15) analyzed the main rotor wake characteristics using CFD. However, both studies were focused on conventional rotor arrangements. Finally, addressing the far wake of quadcopters for the first time, the pioneering studies by Wang et al. (Refs. 16, 17) presented preliminary results of the CFD simulation of quadcopter wakes. The authors simulated the encounter of a multi-rotor UAS wake by another UAS to evaluate the related hazard. They also proposed a preliminary characterization of the effect of the drone fuselage on the wake development. The underlying simulation framework is however based on a steady vorticity generation process that can lead to different wake vortex characteristics than those from actual rotors. An alternate method was presented by the same authors in Ref. 18, combining RANS and LES simulations and accounting for the intrinsic unsteadiness of the flow.

In this work, we present a numerical procedure to simulate the wake of any rotary vehicle, all the way down to the very far wake. The procedure combines space- and time-developing simulation paradigms, giving access to the wake over unprecedented distances at a limited computational cost. We employ this novel procedure in combination with a Vortex Particle–Mesh (VPM) method to measure and compare the wake characteristics of the three UAM vehicle concepts shown in Fig. 1, in cruise conditions. Finally, we present a reduced-order model of the wake which combines information from existing models of the vortex total circulation, core radius, and circulation distribution. We compare the resulting predictions with our simulation results. The proposed composite model could eventually be used inside a UTM framework for the determination of safe separation distances.

This paper is organized as follows. First, we present the numerical procedure and the related large eddy simulation tools. In a follow-up section, we detail the UAM vehicle models and the operating conditions used for the simulations. The simulation results are then presented. We analyze the near wake topology, and we measure and compare the wake properties down to the far-wake. Informed by our measurements, we fit the reduced-order wake model to the temporal and spatial evolution of the circulation distribution. Finally, we close the paper with some concluding remarks.

METHODS

Two-stage Wake Simulation Procedure

A challenging aspect of the wake simulation of rotary vehicles lies in the wide range of space and time scales that must be accounted for. On the one hand, obtaining the near wake requires capturing the rotor aerodynamics, and the ensuing wake generation and roll-up processes. For a wing, the roll-up typically occurs over the first 10 spans downstream of the vehicle. On the other hand, retrieving the far-wake properties

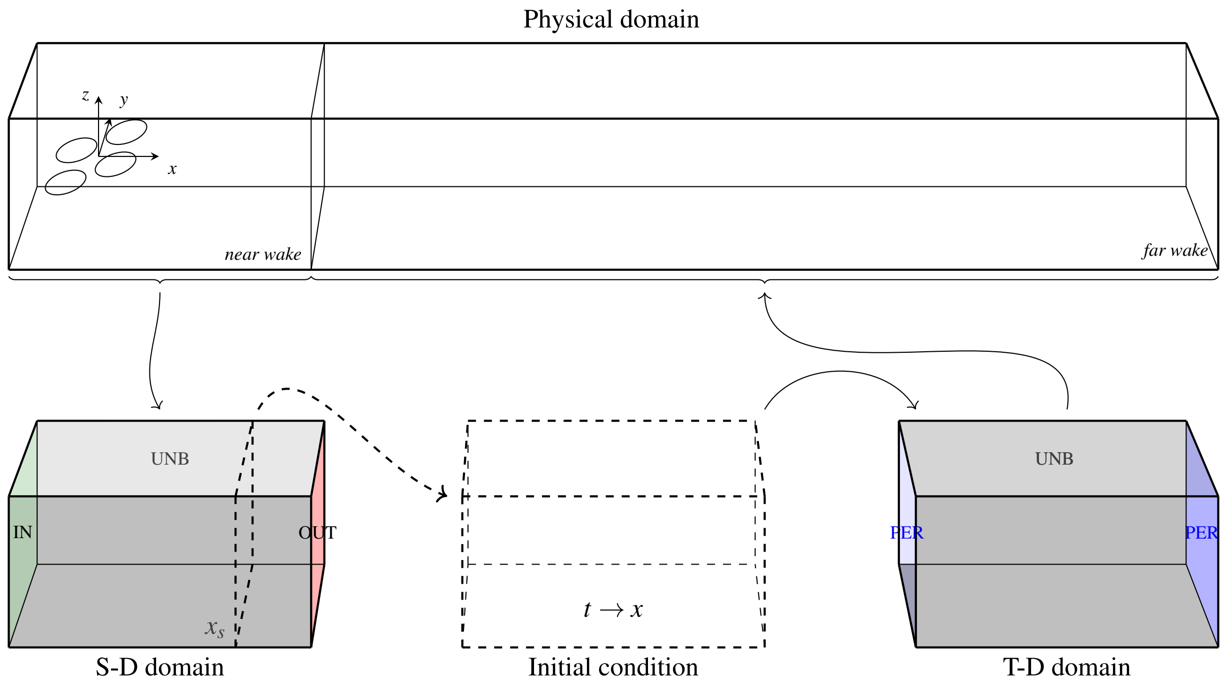

Figure 2: Schematic of the two-stage approach to wake simulation, using a combination of space-developing (S-D) and time-developing (T-D) simulations.

and their evolution over space calls for very long observation domains, up to a couple hundreds spans downstream. Consequently, wake simulations can become cumbersome and require extensive computational resources.

To circumvent this issue and limit the computational burden, we introduce a two-stage simulation approach founded on the observation that a wake can be divided into two regions: the near wake and the far wake. The near wake covers the direct vicinity of the object under investigation where the vorticity is generated and undergoes strong three-dimensional interactions. On the other hand, the far wake is formally defined as the region where the streamwise gradients of vorticity and velocity are small compared to the transverse gradients. This corresponds to a quasi two-dimensional situation where the flow is dominated by the main trailing vortices.

Our numerical procedure mimics this decomposition, as illustrated in Fig. 2. First, the near wake is simulated in a so-called space-developing (S-D) paradigm. One can picture it as the numerical equivalent of a wind tunnel experiment, with a non-zero velocity at the inlet of the computational domain and a static model. Consequently, a potentially unsteady wake develops spatially behind the modeled object. For the far-wake region, we use a time-developing (T-D) paradigm to age the wake vortices. A portion of the S-D wake is first isolated following a procedure explained hereafter. Then, this initial condition is evolved over time in a frame moving in the streamwise direction at a constant velocity equal to the inflow velocity of the S-D simulation. Since the frame is moving, long simulation times correspond to far distances into the wake. The major advantage of this technique is the reduced computational effort since all computations are performed in a relatively small spatial domain, determined by the length of the initial condition. Conversely, if the S-D simulation had to be run down to the far wake, the spatial extent of the domain would need to be as long as the desired wake length (up to several hundreds spans); the simulation time would also be much longer, as the S-D wake would first need to reach the far wake, then the simulation should be continued so that statistics can be collected.

While S-D and T-D paradigms have been used separately in the past for wake simulation (see. e.g. Refs. 15, 16 for S-D examples, and Refs. 19, 20 for T-D), their combined use has been much scarcer. In this work, the connection between S-D and T-D relies on the computation of the initial condition of the T-D simulation that is obtained directly from the S-D simulation, based on a space-time analogy. The vorticity field is recorded over time in a 2D slice of the S-D simulation, located at a chosen downstream location x_s. This 2D, time-dependent information is used to reconstruct a 3D vorticity field where the time t was replaced by a third spatial coordinate x. The "unfolding" of time into space corresponds to sampling the 2D information at a frequency f matching the required spatial resolution dx using the prescribed streamwise velocity U_∞ of the S-D simulation, $f = \frac{U_\infty}{dx}$. This 3D vortex field is then advanced in time in the T-D simulation domain where the third direction is made periodic.

Similar simulation techniques were used by Ning et al. (Ref. 21) and Ransquin et al. (Ref. 22) for the computation of the wake of airplanes flying in formation, although we believe the present work constitutes the first application of the unfolding technique to rotary vehicle wakes. In fact, imposing spatial periodicity in the T-D simulation is quite natural for rotary vehicles. Most likely, the time signal of vorticity recorded in the slice located at x_s is dominated by rotor frequencies and their harmonics. This should be true for moderate x_s, as it was previously shown that the wake progressively loses periodicity when the downstream distance increases (Ref. 15). In the present study, since all rotors rotate at the same frequency, we record the equivalent of 10 revolution periods in the S-D simulation and unfold it into the corresponding periodic length in the T-D simulation. From the T-D simulation, "time-averaged" wake properties are then obtained by computing spatial averages over the periodic direction.

Numerical Flow Solver

In this work, both the S-D and T-D simulations employ the VPM method that enables large eddy simulation of the Navier-Stokes equations. This state-of-the-art CFD method is known for having low dissipation and dispersion errors (Ref. 23), which makes it well-suited for the study of wakes. The aerodynamics of wings and rotors are modeled using lifting lines which take care of shedding the appropriate vorticity in the vicinity of the the lifting surfaces. We refer the reader to our previous publications (Refs. 15, 24 and references therein) for a detailed description of the method.

It is worth noting that the two-stage procedure presented above is general enough to be used with virtually any CFD solver. For this study, we work with the VPM method for its known advantageous numerical properties, and the ease of defining wake-suited boundary conditions. In particular, the S-D simulation uses inflow-outflow boundary conditions in the streamwise direction. They are obtained by applying symmetries on the vorticity field. The T-D simulation is a continuation of the S-D simulation, and uses periodic boundary conditions in the x direction. Recall that the simulation is performed in a frame "moving" at a constant velocity in that direction. Both simulation domains have unbounded boundaries on the sides. More details on the implementation of boundary conditions in the VPM solver can be found in (Ref. 25).

UAM VEHICLE MODELS

In this work, we model three UAM vehicle concepts: the quadcopter (Quad), the side-by-side (SbS) and the lift+cruise (L+C) configurations. All are 6-passenger vehicles, with similar masses and cruise velocities. As these are the two main parameters driving the wake vortex strength, this choice ensures that all wakes have similar initial properties. However, each of these vehicles has a distinct wake generation mechanism that will affect their far wake properties.

As this study focuses on the wake vortices that are primarily due to the lift signature of the vehicle, we limit our model to the main lifting surfaces of each vehicle. The main geometric properties of our models are summarized in Table 1. The operating conditions are described in Table 2. We simulate a single operating point for each vehicle, corresponding to the reported cruise conditions.

For all rotors, the blade twist is linear, with the value indicated in Table 1 measuring the delta between $r = 0$ and $r = R$ (from shaft to tip). The baseline blade pitch is set so that the chord at $r/R = 0.75$ is parallel to the rotor plane. The reference area is here defined arbitrarily as the sum of all rotor areas or the projected wing area. Each vehicle span is measured from tip to tip.

For the Quad and SbS configurations, we used the data published in Refs. 13, 26 and in Ref. 12, respectively. Our models of the vehicles are comprised of the rotor blades only. We do not include the fuselage, or any of the wings and/or struts. One reason for this is that very few details are publicly available about those elements. However, we deem their contribution to the total lift signature of the vehicle is not significant. For example, from visual inspection, the wing area of the SbS configuration amounts to approximately 2 m^2, that is, 3 % of the reference area. Assuming a lift coefficient of 0.5, the wing would add approximately 12 % to the rotor-generated lift.

We simulate the Quad configuration with a rotor lateral spacing of $1.35D$ and vertical spacing of $0.35R$, and the SbS configuration with a rotor lateral spacing of $0.85D$. Regarding operating conditions, γ is the pitch angle of the vehicle (positive nose up). θ_0 is the rotor collective pitch input, and θ_{1c}, θ_{1s} are the cyclic pitch inputs. For the SbS configuration, we prescribe the blade pitching motion to be the same as in the trim conditions reported in the above reference. Similarly, for the Quad configuration, we prescribe the blade flapping motion to the published values. However, to improve the match between the reference lift distribution and our results (discussed below), we added a non-zero control angle θ_{1s} that was not reported in the reference.

The L+C configuration is much more similar to a conventional aircraft. We choose to limit our model of that vehicle to the main wing only. For simplicity, we assume an elliptic lift distribution. The wing pitch (i.e. the geometric angle of attack) is determined empirically so that the total lift falls in the same range as the lift of the two other vehicles. This will allow us to compare the previous rotary configurations to a well-known and simple reference case.

As required for our lifting line model, polars are obtained using XFOIL (Ref. 27) for all airfoils the blades are made of. The airfoil distributions along the rotor blade are detailed in the above references. As the wing of the L+C evolves in steady flow conditions at a moderate incidence, we use a simple polar with a lift slope of 2π.

As a result of the S-D simulations, the polar representation of the lift distribution over the rotors is shown in Fig. 3. The quantity presented is the sectional force coefficient defined as,

$$c_z = \frac{\ell_z}{\frac{1}{2}\rho(R\Omega)^2 c}, \tag{1}$$

where ℓ_z is the local blade sectional force projected along the vertical direction z, and c is the local chord length. The air density is chosen as $\rho = 1.225\ kg/m^3$ for all simulations. Our results in the figure compare qualitatively well to the data shown in Refs. 26 and 12. A more in-depth comparison is

Table 1: Models geometry parameters.

	Quad	SbS	L+C
rotor radius $R = D/2$ $[m]$	2.81	3.20	–
root radius R_i/R	0.12	0.14	–
vehicle span b $[m]$	13.20	11.85	14.70
ref. area S $[m^2]$	99.15	64.46	17.50
rotor separation Δ/D $[-]$	1.35	0.85	–
twist $[°]$	−12.0	−16.0	0.0
blade airfoil	modern thick [a]		2π

[a] private communication, P. Ventura Diaz

Table 2: Operating condition parameters.

	Quad	SbS	L+C
rotation rate Ω $[rpm]$	500.0	500.0	–
flight velocity U_∞ $[m/s]$	62.6	59.2	60.0
advance ratio μ $[-]$	0.418	0.348	–
vehicle pitch γ $[°]$	−11.0	−10.0	4.4
control inputs			
θ_0 $[°]$	15.8, 16.5 [a]	10.0	–
θ_{1c} $[°]$	0.0, 0.0 [a]	3.0	–
θ_{1s} $[°]$	−11.5, −11.5 [a]	−8.5	–
flapping response			
β_0 $[°]$	2.5, 2.6 [a]	3.0	–
β_{1c} $[°]$	−5.1, −5.4 [a]	0.0	–
β_{1s} $[°]$	4.0, 3.3 [a]	0.0	–
total lift[b] L $[kN]$	17.43	17.92	17.65
ref. circulation[b] Γ_0 $[m^2/s]$	20.45	20.02	20.79
ref. spacing[b] b_0 $[m]$	10.89	12.34	11.55
ref. time[b] T_0 $[s]$	36.44	47.77	40.28

[a] first value for front rotors, second value for rear rotors
[b] simulation result

unfortunately not possible because numerical values were not reported in these references.

WAKE RESULTS

We present the results of our two-stage simulations of the three UAM vehicles in cruise conditions. All simulations are run at similar spatial resolutions: $h/D = 1/16$ for the rotary cases, and $h/b = 1/80$ for the L+C, where h is the grid spacing. While relatively coarse, our past experience has shown that such a resolution is sufficient to capture the driving vortex dynamics in the roll-up of the wakes, and their subsequent evolution and decay. Because this study primarily aims to perform a relative comparison between the wakes of the three vehicles, we will highlight the differences in the roll-up mechanisms and compare the wake properties.

The S-D computational domain is set such that the inlet boundary is located just over 1 span upstream of each vehicle, and the outlet boundary at more than 4 spans downstream. The lateral boundaries are automatically adapted so that all the vorticity remains enclosed in the domain. The T-D initial condition is computed based on vorticity recorded at $x_s/b \simeq 2.5$ in the S-D domain. The choice of this location is arbitrary, but informed by the following considerations: x_s must be far enough from the vehicle so that the influence of the bound vorticity on the the vortex dynamics at that location can be neglected. On the other hand, it is desirable to keep a certain distance with respect to the outlet boundary where a symmetry condition is imposed.

Overall, thanks to the relatively coarse resolution of the present simulations, the computational cost is moderate. The S-D simulations took on average 30 core-hours for two convective times (defined by the S-D domain length divided by U_∞). The T-D simulations took on average 1300 core-hours. For reference, the total cost of one simulation (S-D and T-D) is at least one order of magnitude smaller than the simulations we performed in Ref. 15, although those used a finer resolution.

In the remainder of this section, we first describe the wake roll-up mechanisms qualitatively based on direct observations of the flow field. We then perform a quantitative analysis of the wake properties.

Wake Roll-up

An instantaneous representation of the near wakes of all three vehicles is shown in Fig. 4. Each wake presents different characteristics in terms of the initial roll-up mechanism. Starting with the simplest one, the L+C configuration features the expected characteristics of a wing wake. The tip vortices trail from the wing and act to roll up the remainder of the vortex sheet.

The Quad configuration features two pairs of rotors in tandem. Seen from behind, the rotors are markedly separate from each other. In addition to the lateral separation, the front and rear rotors are purposely offset vertically to avoid direct rotor-wake interactions. Consequently, the wake initially behaves as if the wake from each rotor were independent. However, after a short distance (less than 1 span), the wakes from every rotor start mixing.

The SbS exhibits a near wake with a rather different shape. On the one hand, the wake formed from the advancing side is similar to that of a conventional helicopter: the successive blade tip vortices merge to form a rotor “tip vortex” which becomes the main wake vortex further downstream. On the other hand, the overlapping of the rotors triggers immediate vortex interactions between blade tip vortices shed by each

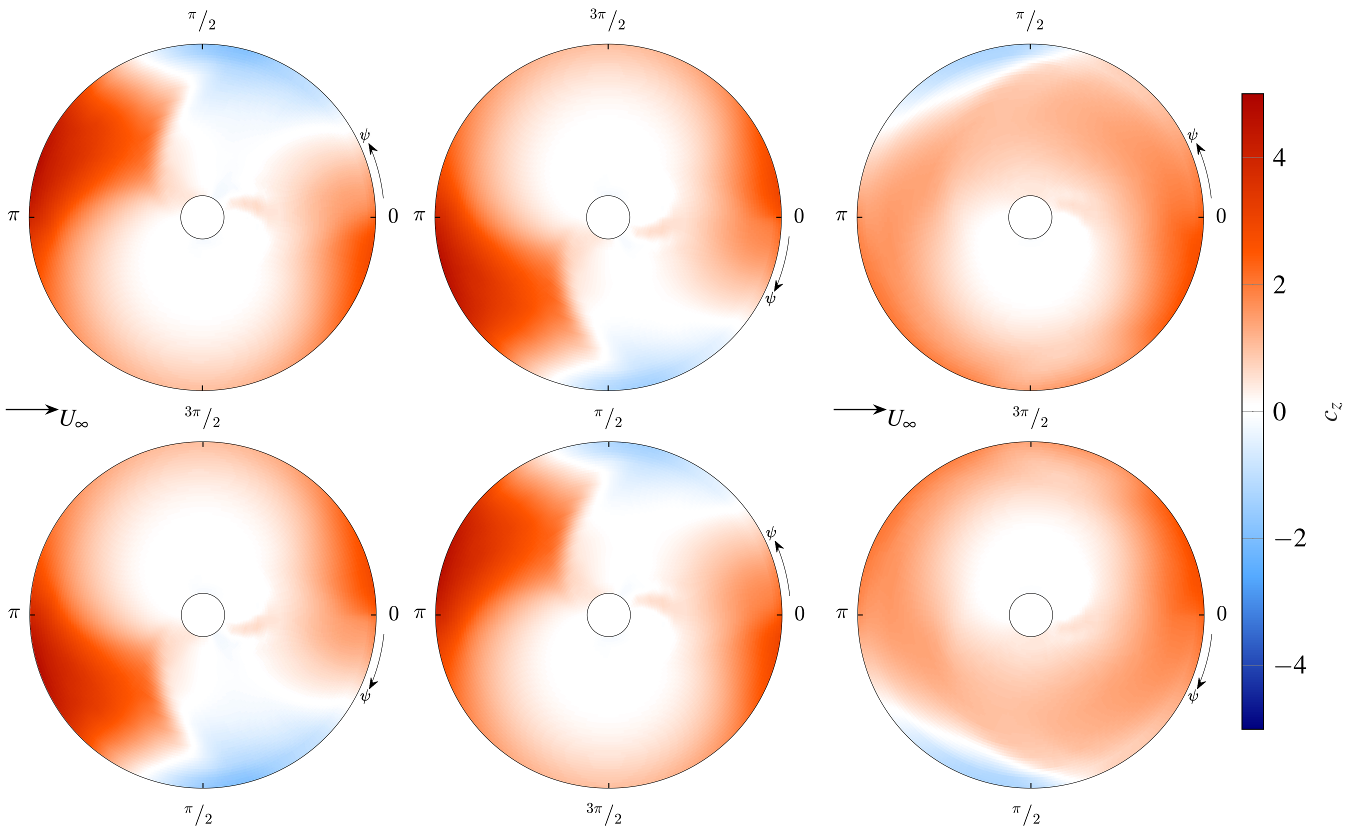

(a) Quad

(b) SbS

Figure 3: Polar representation of the local sectional force coefficient c_z over the rotors of the two rotary configurations.

rotor on their retreating side. As a result, one observes mostly spanwise structures in the central region of the wake right behind the rotors.

In both cases (Quad and SbS), the unsteadiness inherent to the lift generation on the rotor is favorable to the emergence of a fully turbulent wake. This observation was already made in Ref. 15 for a forward-flying isolated rotor. The repeated vortex interactions contribute to creating small vortical structures, through the action of stretching. This is here further exacerbated as the wake of multiple rotors interact with each other.

Additionally, the whole interaction process results in a significant spreading of the forming wake vortices, as compared to the case of the simple wing. This can be more clearly visualized based on the wake slices presented in Fig. 5. It shows the averaged streamwise vorticity $\bar{\omega}_x$ recorded in a slice normal to the x direction at different times. Note that we define the vortex age in terms of the non-dimensional time $T_0 = \frac{b_0}{V_0}$, that is, the approximate time required for the vortex system to travel a distance corresponding to the reference vortex spacing b_0. The reference descent velocity is equal to $V_0 = \frac{1}{2\pi}\frac{\Gamma_0}{b_0}$, where Γ_0 is the reference vortex circulation. Vortex pairs of the same age have thus travelled approximately the same distance. Note that b_0 is unknown apriori for rotary vehicles, and is here chosen based on the results of the simulations. This will be further discussed in the next sections. The numerical values of Γ_0, b_0 and T_0 chosen for this work are reported in Table 2.

Larger coherent vortices are already visible in the early wake stage. The top-most plot row in Fig. 5 shows respectively 4 and 2 larger vortices for the Quad and SbS configuration, shortly after the beginning of the T-D simulation. These larger vortices originate in the rotor "tip" vortices. Note that each rotor seems to produce only one tip vortex, as no large vortex seems to be shed from the retreating side. For the Quad configuration, the trim conditions are such that the rotor loading is lower on the retreating side (see Fig. 3), hence a weaker (almost non-existent) rotor tip vortex on that side. For SbS configuration, the absence of rotor tip vortex at the center of the wake is explained by the rotor overlap which results in the blade tip vortices of the left and right rotors compensating for each other.

A noteworthy feature of the Quad wake is the longer lasting presence of inboard vortices during the roll-up, clearly seen at $t/T_0 = 0.187$. These two structures undergo further turbulent interactions which eventually lead to their mutual destruction. In all three cases, the roll-up eventually produces two axisymmetric trailing vortices, and this process is mostly complete after $t/T_0 = 0.5$.

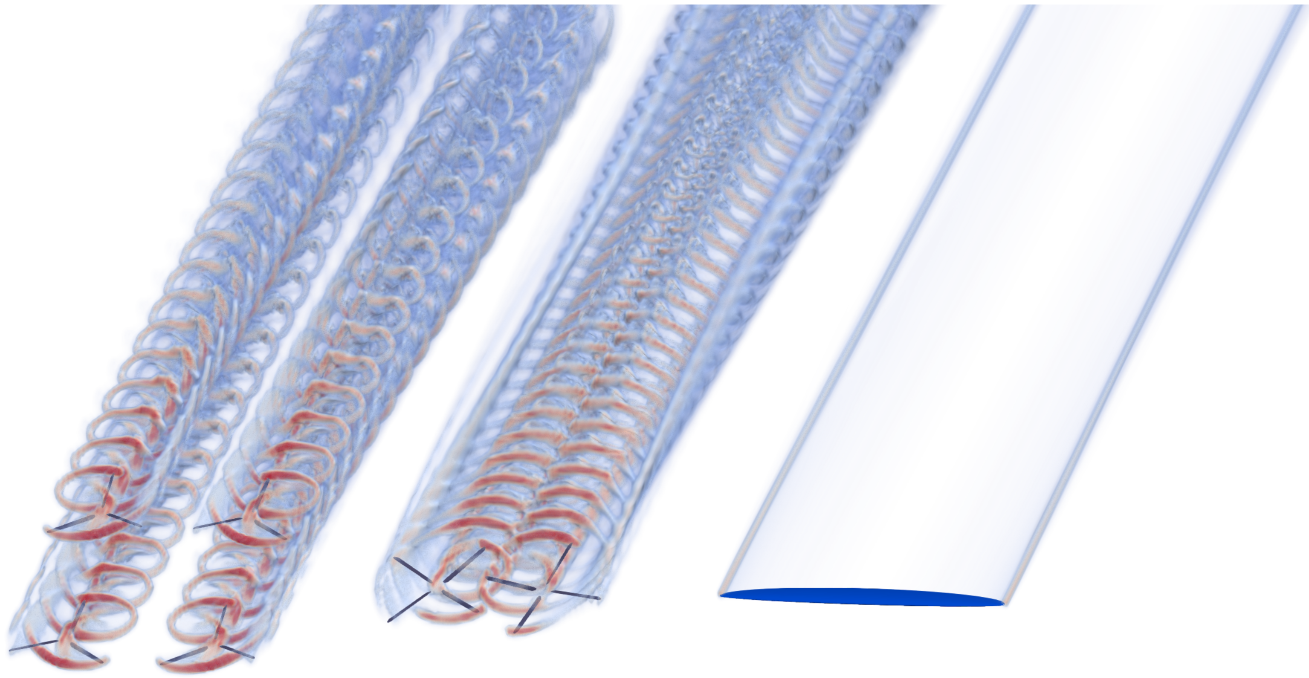

Figure 4: Visualization of the wakes of the Quad, SbS and L+C configurations (from left to right) as a result of the S-D simulation, by volume rendering of the magnitude of the instantaneous vorticity field.

Far Wake Characteristics

Definitions First, we define the wake properties that we measure in the wakes. The reference vertical impulse of the vortex pair $I_0 = \Gamma_0 b_0$ is connected to the total vehicle lift as

$$L = \rho U_\infty I_0. \tag{2}$$

It is thus directly connected to the lift coefficient, $C_L = \frac{I_0}{\frac{1}{2}U_\infty S}$. Γ_0 and b_0 are the reference wake circulation and vortex spacing. Those can be computed analytically only for simple cases such as an elliptical wing. No straightforward definition exist for rotary vehicles, as noted by Teager et al. (Ref. 14), and we shall determine them based on our numerical measurements. The actual vertical impulse of the wake can be measured directly,

$$I_w = \Gamma_w b_w = \int_{-\infty}^{\infty} \left(\int_{-\infty}^{\infty} y\, \bar{\omega}_x \, dy \right) dz, \tag{3}$$

where $\bar{\omega}_x$ denotes the steamwise vorticity averaged over the x direction in the T-D domain. Let us recall that such a spacial average in the T-D simulation corresponds to a time average in the physical domain. We use the computational domain bounds as the bounds of the integrals since the vorticity is compact and entirely contained in the domain. This quantity should be a close enough estimate of I_0 when the descent angle of the wake is small, which is the case here.

The definition of the total wake circulation Γ_w is somewhat arbitrary. Intuitively, it can be captured by computing the integral of the streamwise vorticity in the starboard half plane,

$$\Gamma_w = \int_{-\infty}^{\infty} \int_{0}^{\infty} \bar{\omega}_x \, dy\, dz, \tag{4}$$

provided the wake is symmetric and there is only one wake vortex per half plane. In those conditions, the vortex circulation also likely corresponds to the maximum value of the spanwise circulation distribution,

$$\Gamma_w = \max_y \int_{-\infty}^{\infty} \int_{y}^{\infty} \bar{\omega}_x \, dy\, dz. \tag{5}$$

Note that Eqs.(4) and (5) may yield different results when there are multiple vortices in each half plane, which is initially the case for the rotary vehicles at hand, as seen in Fig. 5. However, as the wake vortices roll up, these two definitions will eventually match. In this work, we opt to compute the wake circulation using Eq. (5). Once the vortex circulation is known, the vortex spacing is determined as $b_w = \frac{I_w}{\Gamma_w}$.

When wake vortices are rolled-up, their circulation distribution is defined as

$$\Gamma(r,t) = \int_0^r \left(\int_0^{2\pi} \bar{\omega}_x(r',t)\, d\theta \right) dr', \tag{6}$$

where t is a measure of the vortex age, and r is the radial location measured from the vortex center. The port and starboard vortex centers are here determined by identifying the location in the slice where the streamwise vorticity component is minimum and maximum, respectively.

The vortex circulation distribution is useful for modeling purposes since the tangential velocity profile is obtained directly from Γ. Assuming the trailing vortices are axisymmetric, we have

$$u_\theta(r,t) = \frac{\Gamma(r,t)}{2\pi r}. \tag{7}$$

The vortex core radius r_c is defined as the radial location where the tangential velocity is maximum.

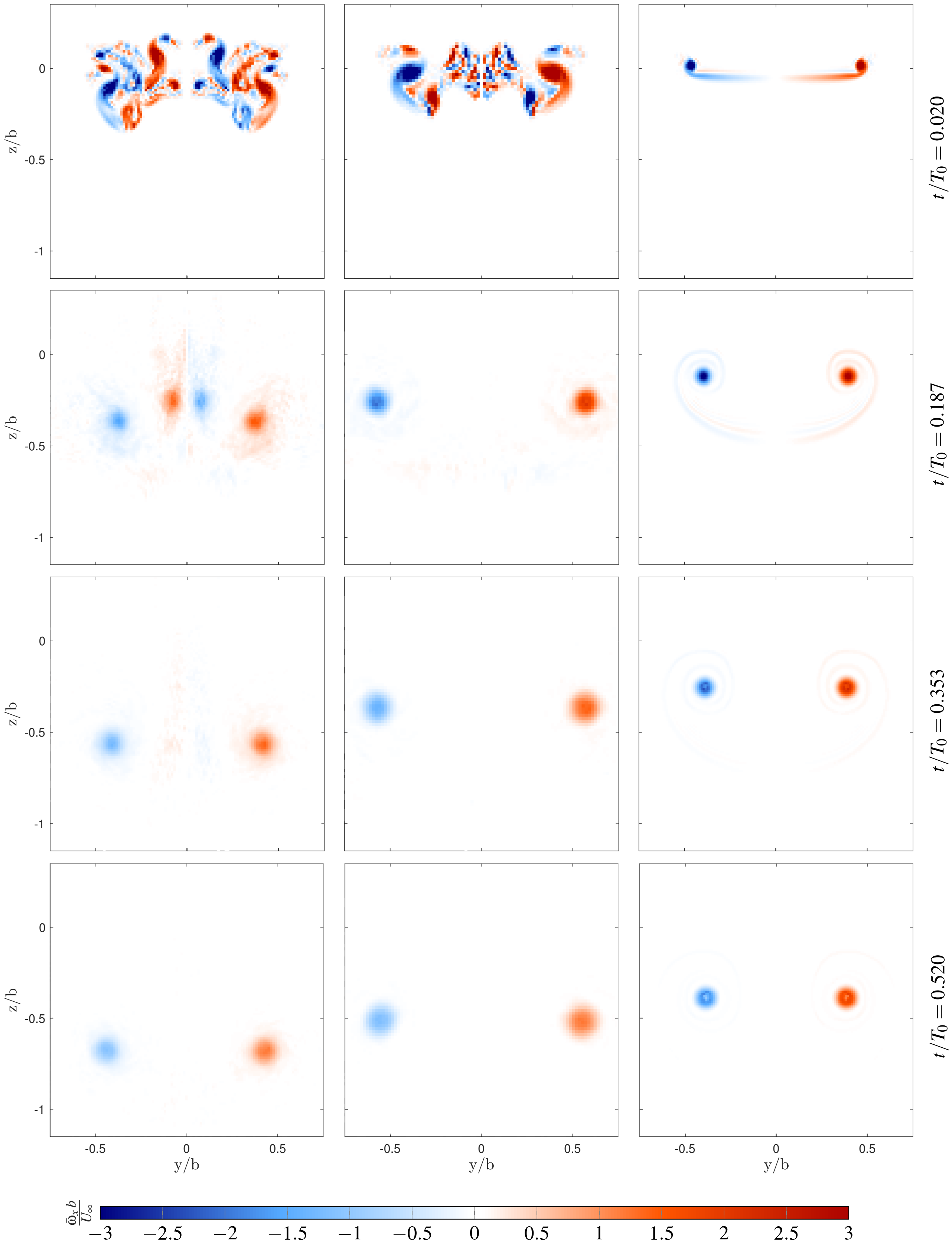

Figure 5: Mean streamwise vorticity in slices of the T-D simulations, at increasing wake ages from top to bottom, behind the Quad (left column), SbS (center column) and L+C (right column).

Finally, we qualify the strength of each wake vortex separately using the measure of the circulation contained in a disk of radius $R^* = b_w/2$ centered on each vortex,

$$\Gamma^* = \Gamma(R^*, t). \tag{8}$$

Note that the total wake circulation Γ_w and the so-defined vortex strength do not necessarily match since some vorticity may be located outside of the disk of radius R^*.

Measurements Figure 6 shows the time evolution of the measured wake properties. The vertical impulse in the wake I_w matches very well the reference impulse I_0 based on each vehicle lift (Fig. 6a) across the whole length of the simulations. This illustrates the good conservation properties of the numerical scheme and hence the adequacy of the VPM method for wake computations.

The vortex spacing b_w is shown in Fig. 6b. It is normalized by the span of each vehicle respectively. After the initial transient due to the roll-up, the spacing of the Quad wake keeps slowly increasing. This may be related to the existence of a net side force on each rotor. We postulate that this side force introduces a distinct lateral component of impulse in the left and right half wake planes, with a net resultant pointing outwards. As a result, the vortex spacing increases linearly over time. For the SbS configuration, the vortex spacing is constant with a value larger than the span measured from tip to tip. This result is not surprising considering the overlap of the rotors. The vortex spacing is still smaller than twice the rotor diameter. Finally, the spacing of the wing wake (L+C) is within 0.6% of the theoretical value for the elliptical wing, $b_0/b = \pi/4$.

From these observations, we define the reference vortex spacing arbitrarily as $b_0/b = 0.825$ for the Quad and $b_0/b = 1.041$ for the SbS. For the L+C, we use the theoretical value. Combining Eq. (2), the total lift measured in the simulation, and the definition of the reference impulse, we obtain Γ_0 presented in Table 1. The values of T_0 directly follows. Consequently, we observe from Fig. 6c that the wake circulations Γ_w normalized by their respective reference circulation is close to 1.0 for all wakes, except during the transient associated with the roll-up. Our choice of b_0 is thus well consistent. Also, as required for the conservation of the impulse, the wake circulation decreases in the Quad wake to balance the increasing spacing.

We now take a closer look at each wake vortex separately: Fig. 7a shows the vortex core radius as a function of their age, and Fig. 7b presents their total circulation. Both quantities further illustrate the previous discussion on the wake roll-up process. First, the spread of the vortex core can be charcterized by the vortex core size. As stated earlier, the rotary vehicles indeed exhibit larger cores compared to the L+C wake vortex as a result of the vortex-induced mixing during the roll-up. Note, however, that the rate of change of r_c after roll-up is similar for all three vehicles. Second, the diffusion of each vortex can be measured based on their circulation. Again, the decrease in vortex strength of the rotary vehicles goes along with a decreasing circulation. Conversely, the wake vortex circulation of the simple wing appears to be almost constant. This behavior is mostly related to the inherent turbulence of each wake. In fact, the L+C wake remains very ”laminar”, whereas the interactions between the tip vortices of the rotary vehicles create smaller and smaller vortical structures, cascading into turbulence. Hence, the turbulent diffusion is higher for the Quad and SbS wakes.

For airplanes, the decay of vortices generally happens in two phases (Ref. 28). The first phase is slow and dominated by a diffusion mechanism, whereas the second is much faster and corresponds to the destruction of the vortices as a result of the growth of Crow instabilities (Ref. 29). Sarpkaya (Ref. 30) showed that the time-to-demise —i.e., the time to reach the second phase— primarily depends on external parameters such as the ambient turbulence and atmospheric stratification.

In this work, our simulations covered the first phase of wake decay, commonly referred to as slow phase decay. From the previous discussion on the vortex strength, we conclude that the diffusion of the circulation is sensitive to the wake roll-up mechansim for rotary vehicles, which itself depends on the vehicle configuration and operating conditions. This is a departure from the wakes of airplanes, where the slow phase decay is relatively insensitive to the total wake circulation and to external perturbations (Ref. 31).

Even though no ambient turbulence is added to our simulations, we surprisingly observe the onset of the Crow instability towards the end of the Quad simulation. Figure 8 shows the typical long wavelength oscillations in the Quad wake vortices, whereas the others are still mostly straight. The higher self-induced turbulence originating in the generation and roll-up mechanisms of the Quad wake may explain why it is the only case where the Crow instability is initiated at $t/T_0 = 2.0$. Further study is needed to characterize the time-to-demise of rotary vehicle wakes and its sensitivity to internal and external conditions.

Modeling Holzäpfel et al. (Ref. 32) proposed the following equation to describe the decay of wake vortices during the slow-phase decay:

$$\frac{\hat{\Gamma}^*(t)}{\Gamma_0} = A_1 - \exp\left(-\frac{R^{*2}}{\nu_1(t-t_1)}\right), \tag{9}$$

where A_1, t_1, ν_1 are tuning parameters. We introduced the notation $\hat{\cdot}$ to denote a modeled quantity.

Models for the vortex core size growth were developed independently. For both helicopter tip vortices (Ref. 33) and airplanes wake vortices (Ref. 34), experimental and mathematical evidence points to a growth that scales with the square root of the vortex age.

Many models for the circulation distribution of vortices also exist. A thorough list of the most common ones used for wake vortices is provided by Gerz et al. (Ref. 35). One model that retains our attention for this study is the multi-scale vortex

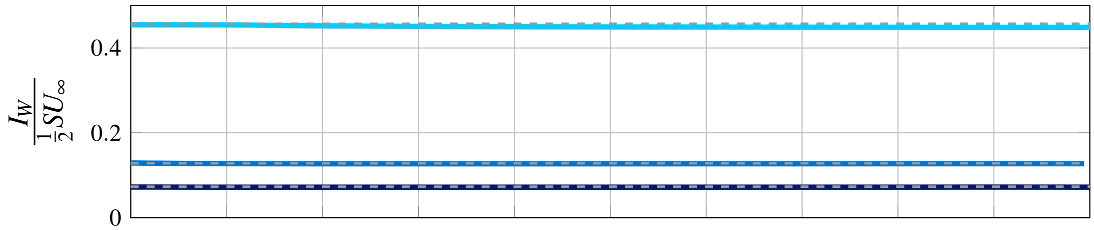

(a) Vertical impulse (solid line). The dashed lines show the reference impulse I_0.

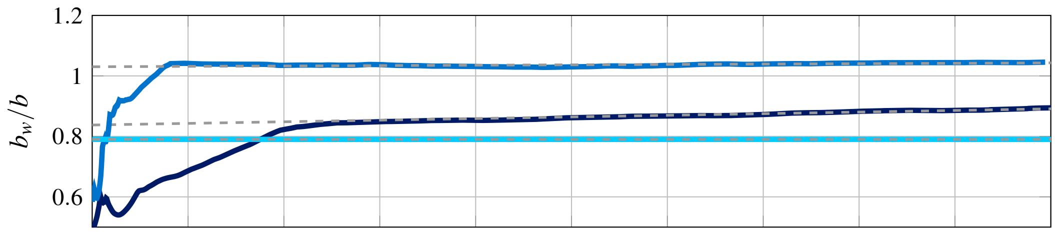

(b) Vortex spacing (solid line). Dashed line shows the result of fitted model.

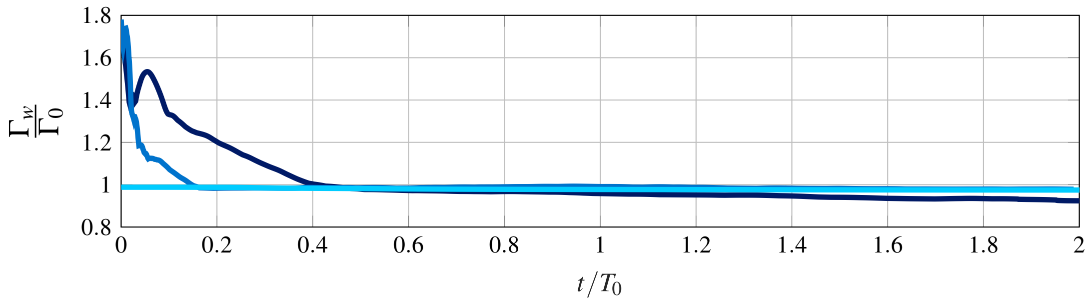

(c) Wake circulation (solid line).

Figure 6: Total wake properties measured in the S-D simulation of the Quad (—), SbS (—) and L+C (—) configurations.

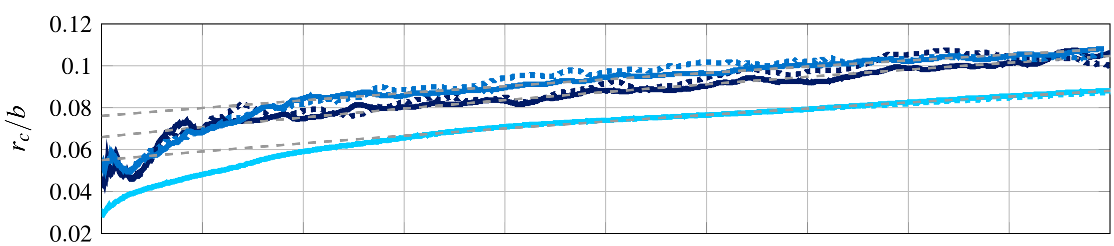

(a) Core size of the port (solid line) and starboard vortex (dotted line).

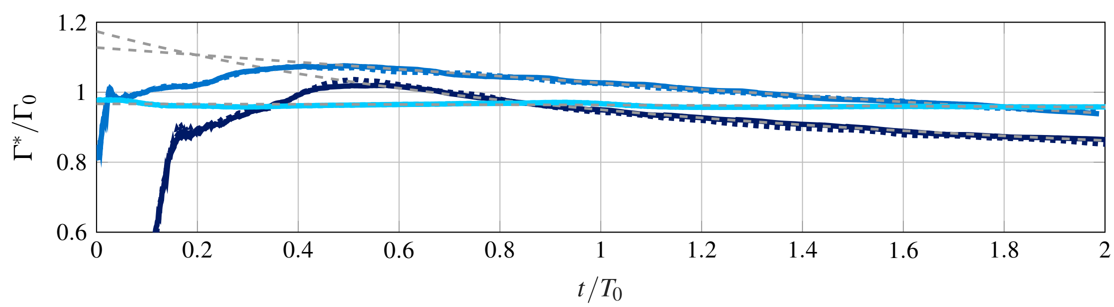

(b) Circulation of the port (solid line) and starboard vortex (dotted line).

Figure 7: Wake vortex properties of the Quad (—), SbS (—) and L+C (—) configurations. The gray dashed lines show the fitted model for the port vortex.

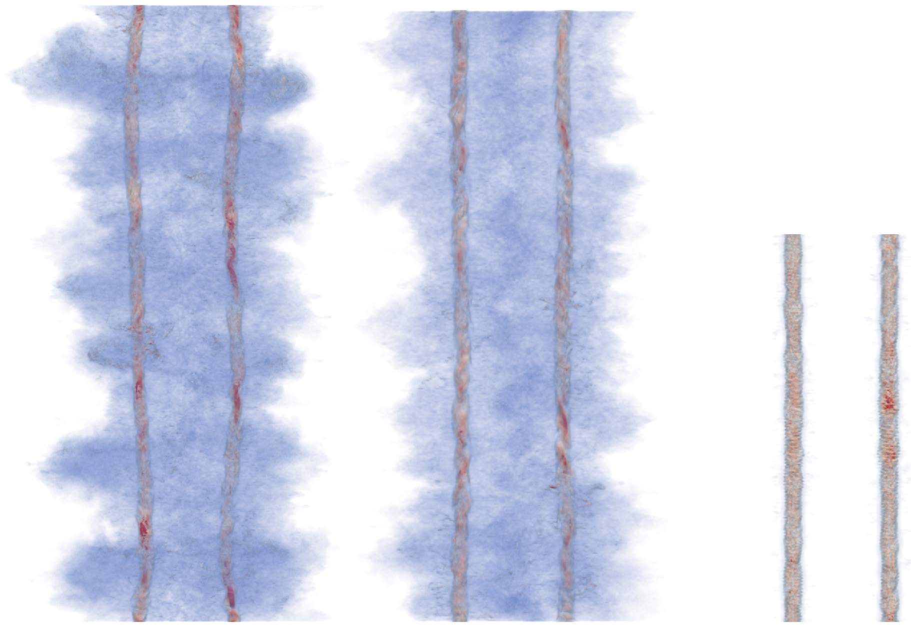

Figure 8: Top view of the wakes of the Quad, SbS and L+C configurations (from left to right) from the T-D simulations at around $t/T_0 = 2.0$, by volume rendering of the vorticity magnitude. Streamwise long-wave oscillations are visible in the Quad wake vortices.

model proposed by Proctor (Ref. 36), and later regularized by Winckelmans (Ref. 34, Appendix B). The original version is a piecewise-defined model enabling the separate description of the inner vortex region, where

$$\frac{\hat{\Gamma}(r)}{\Gamma^*} = 1 - \exp\left(-\left(\frac{r}{\sigma}\right)^2\right), \tag{10}$$

and the outer region, where

$$\frac{\hat{\Gamma}(r)}{\Gamma^*} = 1 - \exp\left(-\left(\frac{r}{\zeta}\right)^{3/4}\right). \tag{11}$$

The parameter σ is the inner length scale and ζ is the outer length scale. Since $\hat{\Gamma}(r)$ is piecewise defined, its derivative is discontinuous at the transition between the two regions. The regularized version of the model solves this issue with the expression:

$$\frac{\hat{\Gamma}(r)}{\Gamma^*} = 1 - \exp\left(-\frac{\left(\frac{r}{\sigma}\right)^2}{\left(1+\left(\frac{\left(\frac{r}{\sigma}\right)^2}{\left(\frac{r}{\zeta}\right)^{3/4}}\right)^q\right)^{1/q}}\right), \tag{12}$$

where q is a blending parameter.

In this work, we combine the above models in order to create a suitable temporal and 2-scale spatial description of the vortex circulation distribution. Our goal is to provide a reasonable estimate that can later be used to compute the induced velocities in wakes. This can be done using the tangential velocity defined in Eq. (7) for each vortex.

We proceed as follows: we first establish three independent fits of Γ^*, r_c and b_w as a function of time. For all three quantities, we employ a standard least-square curve fitting, using the numerical measurements presented above. We exclude the time portion where the wakes are still rolling up, that is, the fits are based on the data range limited to $\frac{t}{T_0} > 0.5$. These fits are then used to inform the circulation distribution model. For this purpose, we slightly adapt the expression of Eq. (12) so as to relate the modeled vortex spacing to the outer scale, $\zeta(t) = a_4 \hat{b}_w(t)$; and the modeled core size to the inner scale, $\sigma(t) = b_4 \hat{r}_c(t)$. a_4, b_4 are constant model parameters to be determined.

A summary of the models and results from curve fitting for the three vehicles at hand is provided in Table 3. A graphic representation of $\hat{\Gamma}^*$, $\hat{r}_c$ and $\hat{b}_w$ is also visible in Figs. 6 and 7. For simplicity, we chose to make a_4 and b_4 independent of the vehicle. The blending parameter q, however, needs to be adjusted as the shape of the distribution depends on the roll-up process, hence on the vehicle. The values of a_4, b_4 and q are determined empirically.

Note that there is roughly one order of magnitude between the c_1 coefficient of the Quad and the SbS configurations, and of the SbS and the L+C. From Eq. (9), we have $c_1 \sim \frac{\nu_1}{R^{*2}}$, hence c_1 is essentially driven by a viscosity. High viscosities again attest to the inherent turbulent diffusion and the faster wake decay of the rotary configurations.

A comparison between the measured and modeled vortex circulation distributions is shown in Fig. 9. The axes are made non-dimensional using the vortex spacing and the wake vortex circulation. The shape of the distributions again depend on the vehicle and reflects the history of the wake. The larger r_c of the Quad implies a weaker gradient of circulation

Table 3: Summary of wake models and fitted parameters.

model		Quad	SbS	L+C	
$\hat{\Gamma}^*(t) = \Gamma_0 \left[a_1 - \exp\left(-\frac{1}{c_1(t-t_1)}\right)\right]$	$a_1 =$	1.66	1.38	0.97	$[-]$
	$t_1 =$	-30.20	-122.46	-200.0	$[s]$
	$c_1 =$	0.0111	0.0014	0.0002	$[s^{-1}]$
$\hat{r}_c(t) = \sqrt{a_2(t-t_2)}$	$a_2 =$	0.0158	0.0087	0.0127	$[m^2 s^{-1}]$
	$t_2 =$	-48.17	-93.79	-51.57	$[s]$
$\hat{b}_0(t) = a_3 t + b_3$	$a_3 =$	0.0097	0.0016	0.0	$[m\,s^{-1}]$
	$b_3 =$	11.06	12.21	11.61	$[m]$
$\hat{\Gamma}(r,t) = \hat{\Gamma}^*(t)\left[1-\exp\left(-\frac{\left(\frac{1}{b_4}\frac{r}{\hat{r}_c(t)}\right)^2}{\left(1+\left(\frac{\left(\frac{1}{b_4}\frac{r}{\hat{r}_c(t)}\right)^2}{\left(\frac{1}{a_4}\frac{r}{\hat{b}_w(t)}\right)^{3/4}}\right)^q\right)^{1/q}}\right)\right]$	$q =$	1.5	3.0	10.0	$[-]$
		$a_4 = 0.08\,[-]$, $b_4 = 0.97\,[-]$			

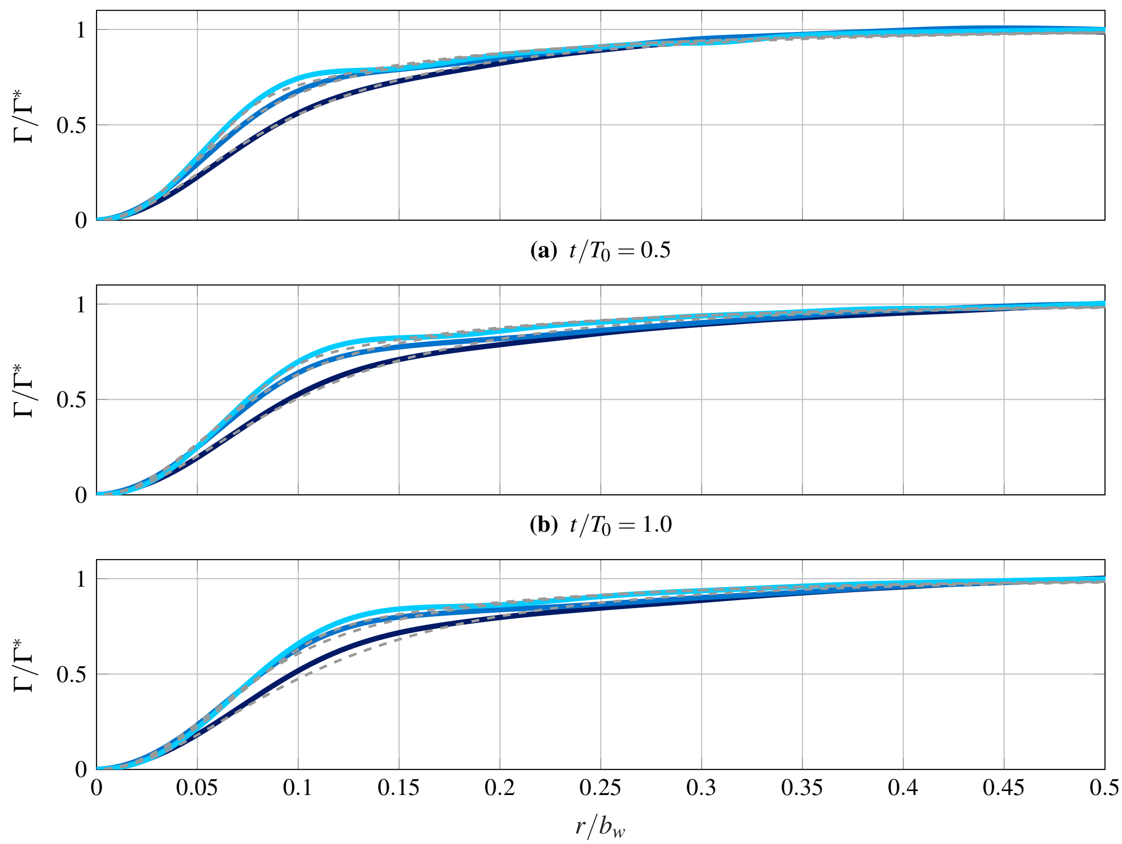

(a) $t/T_0 = 0.5$

(b) $t/T_0 = 1.0$

(c) $t/T_0 = 1.5$

Figure 9: Wake vortex circulation distribution: measurements from the simulations (solid lines) and models (gray dashed lines) for the Quad (—), SbS (—) and L+C (—) configurations.

in the core region, then a faster increase in the outer area. On the other hand, the circulation distribution of the L+C wake vortex increases faster in the cores, but has a smaller gradient in the outer region. Overall, our model of the circulation distribution captures the main trends in the spatial and temporal evolution of the vortex circulation for each vehicle, with a satisfactory agreement. From a modeling perspective, we stress the necessity for using a 2-scale spatial model in order to represent the different behaviors in the core and outer regions.

CONCLUSIONS

In this paper, we have presented a set of simulation and modeling tools for the study of the wakes of arbitrary UAM vehicles. The simulation procedure works in two stages, and can be applied with virtually any CFD method. First, the near wake is computed in a space-developing paradigm. In the second stage, the far wake is aged in a time-developing manner. We showed how periodic information recorded in the former simulation can be used as an initial condition for the latter. This procedure enables the computation of long wake ages at a fraction of the computational cost that would be required if the entire simulation were run in space-developing mode. The modeling effort focused on putting together a reduced-order representation of the spatial and temporal evolution of several wake characteristics. We used previously developed models to fit the vortex spacing, the growth of the core radius, and the wake vortex circulation decay to measurements from the simulations. As an additional modeling step, we proposed a way to combine those three quantities in order to obtain a prediction of the wake vortex circulation distribution. The resulting composite model can be used to predict the wake induced velocities —a necessary quantity for the assessment of the severity of wake vortex encounters.

We have used the simulation tool to compute the wakes of three NASA vehicle concepts over a period corresponding to twice the reference descent time T_0. We have observed that the wakes of rotary vehicles are more complex than the reference case of a wing, which we use to represent the Lift+Cruise configuration. Multiple vortex interactions occur between the blade tip vortices, resulting in self-induced turbulence and a greater spatial spread of the vorticity. We also observed that those wakes take a longer time to roll up. For all vehicles, we determined that the roll-up was completed after $t/T_0 = 0.5$. Consequently, we measured and compared the properties of the rolled-up wake vortices as a function of the wake age. Our analysis showed that the wake of rotary vehicles have larger core radii than the simple wing configuration. Their total circulation also decays faster due to the turbulence generated during wake formation and roll-up. Finally, we verified our modeling approach by applying it to each vehicle's wake. A satisfactory agreement was obtained between the measured and modeled circulation distributions.

The simulation and modeling approaches presented in this paper can be applied to a larger set of vehicle configurations and flight conditions. Only cruise conditions were considered in this work. Another critical condition is the transition to hover: because of the reduced flight velocity, the wake vortices will be more potent, and therefore more dangerous. It is worth noting that while the simulations in this study were performed at similar resolutions for side-by-side comparison, no grid refinement study was performed. Future work will include finer simulations to determine the sensitivity of the wake diagnostics to the spatial resolution. The influence of the small wings and fuselages on wake results should also be assessed to verify our assumption that they can be neglected. Similarly, including the thrusters in the L+C configuration could contribute to generating wake instabilities.

Finally, this study shall be continued to determine the time-to-demise of the wakes in various ambient turbulence conditions. In this study already, we saw first evidence of Crow instabilities in one simulation case, indicating that high self-induced turbulence may help accelerate the wake destruction. This would provide valuable information in the determination of safe separation distances between the various types of UAS traffic in a future UTM framework.

Author contact: Denis-Gabriel Caprace dcaprace@byu.edu, Andrew Ning aning@byu.edu .

ACKNOWLEDGMENTS

The authors express their deep gratitude to Profs. Philippe Chatelain and Grégoire Winckelmans (UCLouvain, Belgium) for providing access to the source code of *VPM4x*. They are also thankful for the computing resources provided by the Office of Research Computing at Brigham Young University. These external contributions enabled the numerical simulations presented in this work.

REFERENCES

1. Bharadwaj, S., Wongpiromsarn, T., Neogi, N., Muffoletto, J., and Topcu, U., "Minimum-Violation Traffic Management for Urban Air Mobility," NASA Formal Methods, edited by A. Dutle, M. M. Moscato, L. Titolo, C. A. Muñoz, and I. Perez, 2021.

2. Verma, S. A., Monheim, S. C., Moolchandani, K. A., Pradeep, P., Cheng, A. W., Thipphavong, D. P., Dulchinos, V. L., Arneson, H., Lauderdale, T. A., Bosson, C. S., *et al.*, "Lessons learned: using UTM paradigm for urban air mobility operations," 2020 AIAA/IEEE 39th Digital Avionics Systems Conference (DASC), 2020.

3. Ivashchuk, O., and Ostroumov, I., "Separation Minimums for Urban Air Mobility," 2021 11th International Conference on Advanced Computer Information Technologies (ACIT), 2021. DOI: 10.1109/ACIT52158.2021.9548355

4. Silva, C., Johnson, W. R., Solis, E., Patterson, M. D., and Antcliff, K. R., "VTOL Urban Air Mobility Concept Vehicles for Technology Development," 2018 Aviation Technology, Integration, and Operations Conference, 2018. DOI: 10.2514/6.2018-3847

5. Johnson, W., Silva, C., and Solis, E., "Concept vehicles for VTOL air taxi operations," AHS Technical Conference on Aeromechanics Design for Transformative Vertical Flight, San Francisco, CA, January 16–19, 2018.

6. Johnson, W., and Silva, C., "Observations from exploration of vtol urban air mobility designs," The Asian/Australian Rotorcraft Forum, October 30 – November 1 2018.

7. Nguyen, N. T., "A Physics-Based Spatial Wake Interactional Model of Fixed-Wing Aircraft and Rotorcraft for Urban Air Mobility," AIAA Scitech 2021 Forum, 2021. DOI: 10.2514/6.2021-0881

8. Nguyen, N. T., Bartolini, G., Baculi, J. E., Okolo, W., and Xiong, J., "Wake Vortex Interaction of Urban Air Mobility Aircraft," AIAA SCITECH 2022 Forum, 2022. DOI: 10.2514/6.2022-1031

9. Sheng, C., and Narramore, J. C., "Computational Simulation and Analysis of Bell Boeing Quad Tiltrotor Aero Interaction," *Journal of the American Helicopter Society*, Vol. 54, (4), 2009, pp. 42002. DOI: doi:10.4050/JAHS.54.042002

10. Zanotti, A., Savino, A., Palazzi, M., Tugnoli, M., and Muscarello, V., "Assessment of a Mid-Fidelity Numerical Approach for the Investigation of Tiltrotor Aerodynamics," *Applied Sciences*, Vol. 11, (8), 2021. DOI: 10.3390/app11083385

11. Pinti, O., Oberai, A. A., Healy, R., Niemiec, R. J., and Gandhi, F., "Multi-Fidelity Approach to Predicting Multi-Rotor Aerodynamic Interactions," *AIAA Journal*, , (article in advance), 2022, pp. 1–15. DOI: 10.2514/1.J060227

12. Ventura Diaz, P., Johnson, W., Ahmad, J., and Yoon, S., "The Side-by-Side Urban Air Taxi Concept," AIAA Aviation 2019 Forum, 2019. DOI: 10.2514/6.2019-2828

13. Ventura Diaz, P., and Yoon, S., "Computational Study of NASA's Quadrotor Urban Air Taxi Concept," AIAA Scitech 2020 Forum, 2020. DOI: 10.2514/6.2020-0302

14. Teager, S. A., Biehl, K. J., Garodz, L. J., Tymczyszym, J. J., and Burnham, D. C., "Flight test investigation of rotorcraft wake vortices in forward flight." Technical Report DOT/FAA/CT-94/117, United States Federal Aviation Administration and Scientific and Engineering Solutions, Inc., February 1996.

15. Caprace, D.-G., Chatelain, P., and Winckelmans, G., "Wakes of rotorcraft in advancing flight: A large eddy simulation study," *Physics of Fluids*, Vol. 32, (8), 2020, pp. 087107. DOI: 10.1063/5.0015162

16. Wang, C. H. J., Nathanael, J. C., Ng, E. M., Ng, B. F., and Low, K. H., "Framework for the Estimation of Safe Wake Separation Distance between Same-Track Multi-Rotor UAS," AIAA Scitech 2021 Forum, 2021. DOI: 10.2514/6.2021-0708

17. Wang, C. H. J., Nathanael, J. C., and Low, K. H., "Numerical Investigation on Influence of Fuselage on Multirotor Wake Vortex Structures in Forward Flight," AIAA SCITECH 2022 Forum, 2022. DOI: 10.2514/6.2022-0151

18. Nathanael, J. C., Wang, C. H. J., and Low, K. H., "A Study on Circulation Strength Decay Over Time of Quadrotor Wake Using Large Eddy Simulation," AIAA SCITECH 2022 Forum, 2022. DOI: 10.2514/6.2022-0155

19. Crouch, J. D., Miller, G. D., and Spalart, P. R., "Active-control system for breakup of airplane trailing vortices," *AIAA Journal*, Vol. 39, (12), Dec 2001, pp. 2374–2381.

20. De Visscher, I., Bricteux, L., and Winckelmans, G., "Aircraft vortices in stably stratified and weakly turbulent atmospheres: simulation and modeling," *AIAA Journal*, Vol. 51, (3), 2013, pp. 551–566. DOI: 10.2514/1.J051742

21. Ning, A., Flanzer, T. C., and Kroo, I. M., "Aerodynamic performance of extended formation flight," *Journal of Aircraft*, Vol. 48, (3), 2011, pp. 855–865. DOI: 10.2514/1.C031046

22. Ransquin, I., Duponcheel, M., and Chatelain, P., "Dynamics of the Wake Vortices of a Two-aircraft Formation, Hazard Assessment at Large Distances and Sensitivity Analysis," AIAA SCITECH 2022 Forum, 2022. DOI: 10.2514/6.2022-1198

23. Mimeau, C., and Mortazavi, I., "A Review of Vortex Methods and Their Applications: From Creation to Recent Advances," *Fluids*, Vol. 6, (2), 2021. DOI: 10.3390/fluids6020068

24. Caprace, D.-G., Winckelmans, G., and Chatelain, P., "Assessment of the Vortex Particle-Mesh Method for Efficient LES of Hovering Rotors and their Wakes," AIAA Scitech 2021 Forum, 2021. DOI: 10.2514/6.2021-0738

25. Caprace, D.-G., Gillis, T., and Chatelain, P., "FLUPS: A Fourier-Based Library of Unbounded Poisson Solvers," *SIAM Journal on Scientific Computing*, Vol. 43, (1), January 2021, pp. C31–C60. DOI: 10.1137/19M1303848

26. Ventura-Diaz, P., and Yoon, S., "High-Fidelity Simulations of a Quadrotor Vehicle for Urban Air Mobility," AIAA SCITECH 2022 Forum, 2022. DOI: 10.2514/6.2022-0152

27. Drela, M., "XFOIL: An analysis and design system for low Reynolds number airfoils," *Low Reynolds number aerodynamics*, Springer, 1989, pp. 1–12.

28. Spalart, P. R., "Airplane Trailing Vortices," *Annual Review of Fluid Mechanics*, Vol. 30, (1), 1998, pp. 107–138. DOI: 10.1146/annurev.fluid.30.1.107

29. Crow, S. C., "Stability theory for a pair of trailing vortices," *AIAA Journal*, Vol. 8, (12), 1970, pp. 2172–2179. DOI: 10.2514/3.6083

30. Sarpkaya, T., "Decay of wake vortices of large aircraft," *AIAA journal*, Vol. 36, (9), 1998, pp. 1671–1679. DOI: 10.2514/2.570

31. Holzäpfel, F., "Effects of environmental and aircraft parameters on wake vortex behavior," *Journal of Aircraft*, Vol. 51, (5), 2014, pp. 1490–1500. DOI: 10.2514/1.C032366

32. Holzäpfel, F., Gerz, T., and Baumann, R., "The turbulent decay of trailing vortex pairs in stably stratified environments," *Aerospace Science and Technology*, Vol. 5, (2), 2001, pp. 95–108. DOI: 10.1016/S1270-9638(00)01090-7

33. Ramasamy, M., and Leishman, J. G., "Interdependence of Diffusion and Straining of Helicopter Blade Tip Vortices," *Journal of Aircraft*, Vol. 41, (5), 2004, pp. 1014–1024. DOI: 10.2514/1.3364

34. de Bruin, A., and Winckelmans, G., "Cross-flow kinetic energy and core size growth of analytically defined wake vortex pairs," Technical Report NLR-CR-2005-412, National Aerospace Laboratory NLR, 2005.

35. Gerz, T., Holzäpfel, F., and Darracq, D., "Commercial aircraft wake vortices," *Progress in Aerospace Sciences*, Vol. 38, (3), 2002, pp. 181–208. DOI: 10.1016/S0376-0421(02)00004-0

36. Proctor, F., "The NASA-Langley wake vortex modelling effort in support of an operational aircraft spacing system," 36th AIAA Aerospace Sciences Meeting and Exhibit, 1998. DOI: 10.2514/6.1998-589